ACS NANO

www.acsnano.org

Article

Multimodal DNA Nanostructure Barcodes for Single-Cell Protein Profiling and Tumor Subtyping

Meirong Cui, Chenxu Hu, Jiahan Dong, Yiyu Cheng, Bicheng Sun, Chunhai Fan, Lianhui Wang, and Jie Chao*

Cite This: *ACS Nano* 2026, 20, 5904−5917

Read Online

ACCESS | Metrics & More | Article Recommendations | Supporting Information

ABSTRACT: Molecular classification of diseases that accurately reflects clinical behavior is fundamental to the realization of precision medicine. Single-cell protein analysis combined with coding technology offers a promising approach for constructing robust molecular classifiers. However, the low abundance of disease-related cells and the technical challenges in parallel profiling of multiple proteins remain major obstacles. Herein, we present a DNA nanostructure-based multicomponent coding strategy that enables multiprotein analysis at the single-cell level by precisely controlling the stoichiometry, orientation, and modularity of the magnetized tags and multicolor fluorescent tags. Compared with conventional linear DNA barcoding methods, our approach allows for the simultaneous magnetic separation of heterogeneous cell populations and multicolor fluorescence-based phenotypic encoding. By integrating single-cell trapping techniques, we demonstrate the accurate molecular subtyping of breast cancer based on fluorescence-encoded phenotypic features. This strategy expands the scope of applications in cell sorting, proteomic profiling, and genomic analysis, thus advancing the frontiers of precision medicine.

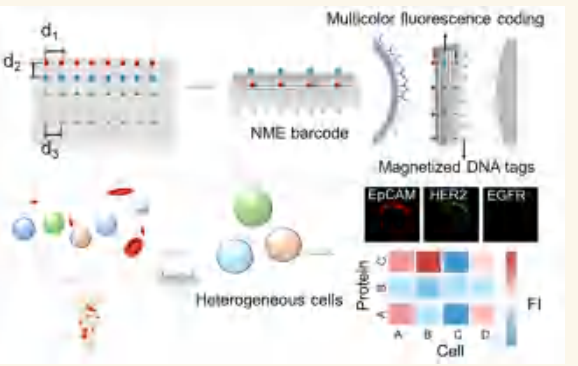

KEYWORDS: *DNA nanostructure, single-cell analysis, multiprotein profiling, tumor subtyping, DNA barcodes, magnetic separation*

INTRODUCTION

Precision medicine requires the development of disease-specific molecular classification methods that accurately reflect clinical behavior.[1,2] Single-cell analysis serves as an excellent method capable of characterizing intercellular heterogeneity resulting from stochastic gene, protein, and metabolite expression.[3] Comprehensive analysis of protein expression and distribution at the cellular level holds immense potential for early disease detection, identification of biological drug targets, and personalized therapy selection.[4−6] Notably, more than 60% of clinically approved drug targets are cell surface proteins. Multiplexed profiling of surface receptor proteins on heterogeneous tumor cells at the single-cell level can significantly enhance cancer precision therapy.[7] Although high-throughput single-cell RNA sequencing has revolutionized our understanding of complex cellular ecosystems, comprehensive characterization of cell phenotypes, particularly through multiprotein profiling, remains a formidable challenge.[8]

Biological systems execute signal transduction and regulate biofunctions by encoding information to individual biopolymers with one-dimensional sequences of nucleotides or amino acids.[9] Advances in the design of synthetic barcodes based on simulated programmable interactions have great potential for the research of biological systems.[10,11] With the advent of encoding techniques, including graphical encoding, chemical encoding, electronic encoding, physical encoding, magnetic encoding, and optical encoding, the parallel detection of multiple biomolecules has been achieved, significantly enhancing sample processing and analysis efficiency.[12−14] However, conventional coding techniques in parallel detection are restricted to identifying targets with only one distinguishing feature (such as gene sequence detection, antigen identification, virus recognition, etc.) and cannot achieve single-cell level analysis of heterogeneous cells with multiprotein expression.[15] Furthermore, the low abundance of disease-associated cells, such as circulating tumor cells and tumor stem cells, and their heterogeneity, impede the classification of cells.[16] Therefore, they are not suitable for routine laboratory detection or clinical application of the cell phenotype. Fluorescence-encoded magnetic nanoparticle−antibody nanoprobes have been designed for analyzing the phenotype of heterogeneous circulating tumor cells in situ, which provides a great tool for the application of fluorescence-encoded multiprotein detection.[17] However, the current

Received: November 2, 2025
Revised: February 4, 2026
Accepted: February 5, 2026
Published: February 12, 2026

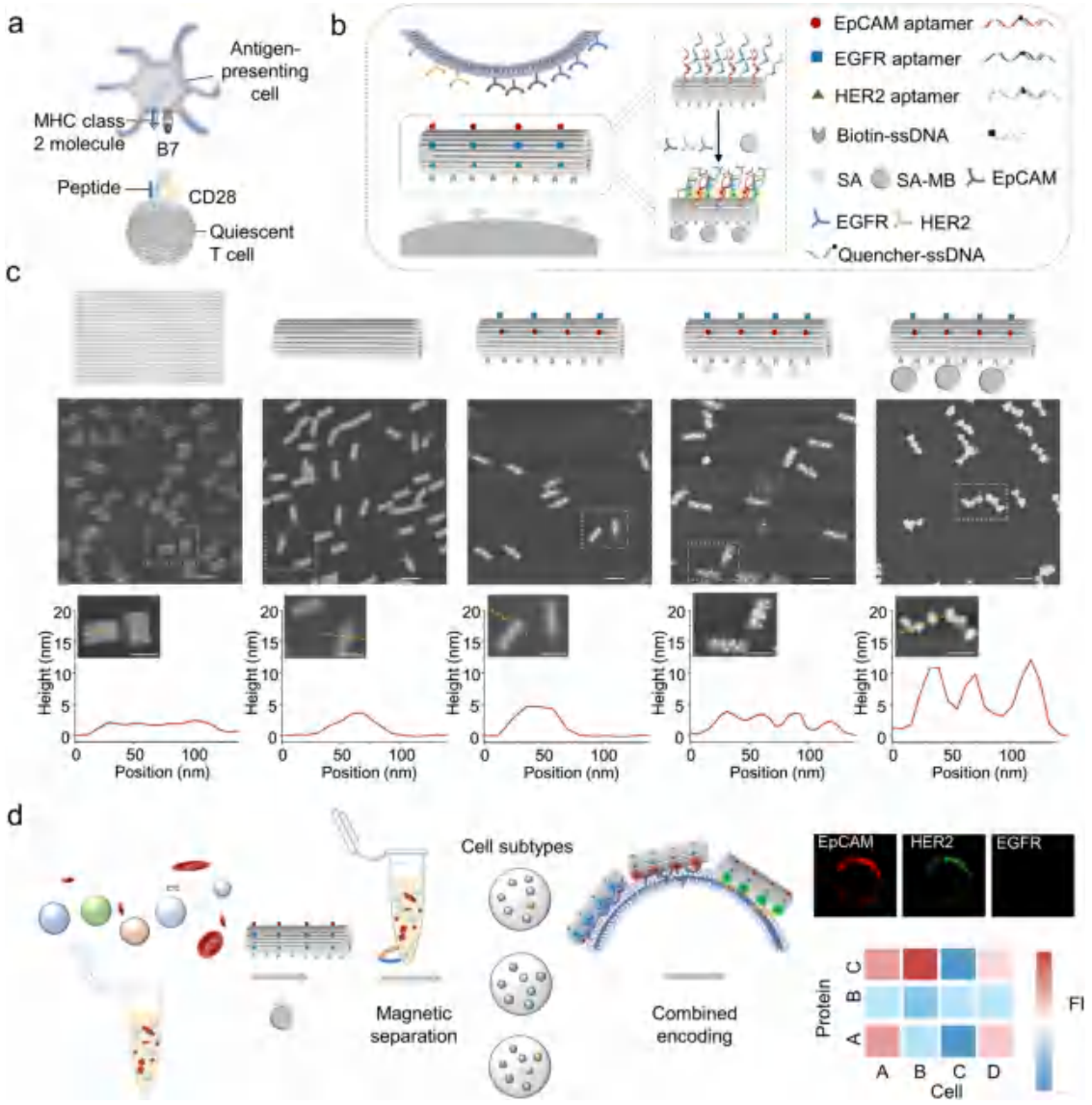

Figure 1. DNA nanostructure-multicomponent-encoded barcodes for profiling multiproteins at the single-cell level. (a) A profile view depicts the T-cell immune synapses' composition and key ligands, enabling the accurate recognition of target cells. (b) Illustration of the construction of NME barcodes and their specific compositions. (c) Schematic and representative AFM images (top and middle rows) and corresponding height profiles (bottom row) showing the stepwise assembly of the NME barcode. From left to right: bare DNA nanotube, bare DNA rectangle, and DNA nanotube nanostructure, DNA nanotube modified with aptamer arrays, the biotin-DNA array-modified nanotubes incubated with SA and SA-MB. Scale bars: 100 nm. (d) Schematic of NME barcodes achieved simultaneous separation of heterogeneous cells and multicolor fluorescent combination coding phenotypes.

barcodes still lack integration and flexibility, and the design of multifunctional barcodes with precise control of stoichiometry, orientation, and modularization for molecular typing by simultaneously recognizing multiple proteins on the cell surface still faces challenges.

DNA barcoding technology provides an attractive approach for gene, protein, and cell-level analysis.[18−22] The programmability and addressability of DNA nanostructures enable researchers to precisely position organic fluorophores and other functional molecules within a well-defined nanoarray. This capability allows for the construction of DNA-based magnetic, fluorescent, or chemical barcodes, greatly expanding the range of applications for barcodes.[23−26] Aside from the primary structure of the DNA sequence, the specific nature of Watson−Crick base pairing dictates that DNA folds into specific three-dimensional topologies.[27−30] Especially, the number, relative distance, and composition of the modified functional molecules on DNA topologies can be well controlled, which enhances the discrimination ability of barcodes and can be used for multiplexing analysis.[31−34] DNA coding strategies have been applied for the analysis of multiple protein profiles in single cells in recent years, enabling the realization of parallel detection of multiple discriminant modules.[35,36] However, DNA barcodes still encounter challenges in performing multiple functions simultaneously, such as the efficient isolation and phenotypic analysis of heterogeneous cells at a single-cell level based on multiplex biomarker profiling. While powerful techniques like CITE-seq (Cellular Indexing of Transcriptomes and Epitopes by Sequencing), REAP-seq (RNA Expression and Protein Sequencing assay), and CyTOF (Cytometry by Time-Of-Flight) enable deep, high-plex protein profiling, they often require preenriched cell populations and do not inherently

https://doi.org/10.1021/acsnano.5c18968
ACS Nano 2026, 20, 5904−5917

integrate a cell capture mechanism. This presents a challenge for analyzing extremely rare cells, such as CTCs, which can be lost during sample preparation or upstream sorting processes. Therefore, there remains a critical need for an integrated platform that can first efficiently isolate these rare cells from complex biological samples and then perform multiplexed profiling.

Harnessing sequence−structure synergy, we developed a DNA nanostructure-multicomponent-encoded barcode system (termed NME barcodes) capable of both magnetic separation and multicolor fluorescence phenotyping of heterogeneous cells. Inspired by the spatial organization of immune and tumor cell receptors, we employ DNA origami to integrate DNA nanotubes with predesigned magnetized tags and multicolor fluorescent tags. (Figure 1a,b). Considering the significance of pivotal biomarkers, such as epithelial cell adhesion molecule (EpCAM), epidermal growth factor receptor (EGFR), and human epidermal growth factor receptor-2 (HER2) in predicting patient survival and personalized cancer treatment, these three membrane proteins were selected as targets to validate NME barcodes for single-cell multiprotein analysis and heterogeneous cell classification.[37−39] Particularly, the barcodes achieved precise control over the stoichiometry, orientation, and modularity of magnetized tags and multicolor fluorescent tags on the DNA nanotube nanostructures (Figure 1c). The programmed structural configuration significantly improved the parallel detection capability of multicolor fluorescence coding at the molecular nanoscale level. Combined with magnetic separation and immunofluorescence analysis, multicolor fluorescence aptamer arrays on DNA nanotubes enable the efficient targeting and profiling of multiple protein clusters on tumor cell surfaces with high phenotypic heterogeneity. Through qualitative and quantitative analyses of fluorescence-encoded signals obtained via fluorescence microscopy, we performed a detailed phenotypic analysis at the single-cell level (Figure 1d). Compared with linear DNA barcoding, our barcodes enable the simultaneous separation of heterogeneous cells and multicolor fluorescent combination coding phenotypes. This interdisciplinary strategy creates a universal, intelligent, and modular nanoplatform for multiplex bioassays, such as cell sorting, proteomics, and genomics.

RESULTS AND DISCUSSION

Design Principle

The modular design of barcodes is composed of DNA nanotubes, magnetized DNA tag arrays, and multicolor fluorescent aptamer arrays. We assembled DNA nanotubes using ∼7000 base circular single-stranded M13 DNA and 216 short staple strands through a single annealing step. The DNA nanotube was obtained by adjusting the sequence of the long edge chains of the rectangular origami nanostructure (DNA nanosheet) (Figures S1 and S2). To build the modular DNA origami nanostructure nanoarrays, four types of short staple strands were combined with core sequences and variable overhangs at designated positions on the DNA origami surface for subsequent modification (Figures S3 and 1b). Three specific fluorophore-modified aptamer arrays targeting EpCAM, HER2, and EGFR clusters (receptor membrane proteins distributed in high-order cluster structures, the diameter of most EpCAM clusters, HER2 clusters, and EGFR clusters in tumor cells are in the range of ∼30−70 nm, ∼67 nm, ∼70−660 nm, respectively[40,41]) were bound with the designated overhangs on the DNA nanotube. These three aptamer arrays targeting EpCAM, EGFR, and HER2 were labeled with Alexa Fluor 647, Alexa Fluor 561, and Alexa Fluor 488, respectively. The fluorescence intensity of the aptamer arrays can be quenched by partially complementary single-strand DNA strands (quencher ssDNA) and recovered upon binding to the corresponding receptor protein clusters on the membranes of heterogeneous cells. The biotin-modified DNA arrays were encoded as magnetized tags positioned on the reverse side of the aptamer arrays on the nanotube, enabling subsequent binding with streptavidin-functional magnetic beads (SA-MB) for the magnetic separation of single cells. Therefore, barcodes can be used for the simultaneous separation of heterogeneous cells and multicolor fluorescent combination coding phenotypes.

The step assembly of NME barcodes was investigated by atomic force microscopy (AFM) and agarose gel electrophoresis. As shown in Figure 1c, measured from the structure of the annealed DNA nanostructure, the length of both the tube and the rectangle was ∼100 nm, which was consistent with the theoretical reported data.[42−44] To demonstrate the assembly of the biotin-modified DNA arrays on the designed site of the DNA nanotube, the biotin-DNA array-modified nanotubes were incubated with SA and SA-MB (diameter of ∼10 nm), respectively. The AFM images of their measured heights demonstrated that the magnetized tag array was positioned on the designed site of the nanotube and could subsequently bind with SA and SA-MB for magnetic separation. Agarose gel electrophoresis analysis further indicated the successful construction and stability of the NME barcode in FBS (Figures S4 and S5). Furthermore, the physicochemical properties of the nanostructures were thoroughly characterized. ζ-potential measurements confirmed the progressive functionalization of the barcodes. The analysis of the length distribution of the NME barcode by AFM imaging suggested a monodisperse population with a uniform size consistent with the design, providing further evidence of their successful and homogeneous assembly (Figure S6).

Given that reproducibility and stability are critical for the practical application of DNA nanostructures, we further systematically evaluated the NME barcodes. First, we prepared three independent batches of NME barcodes. Electrophoresis results showed high uniformity across all batches, with structural integrity exceeding 94%, confirming the high reproducibility of our fabrication method (Figure S7a). Concurrently, we assessed the long-term storage stability of the barcodes at 4 °C and found that approximately 75% of the structure remained intact after 7 days (Figure S7b). More importantly, to validate their performance in a complex biological matrix, we tested the stability of the NME barcodes in the whole blood samples. The results revealed that approximately 63% of the barcodes remained intact even after a 12-h incubation (Figure S8), demonstrating excellent resistance to nuclease degradation, which is sufficient for the requirements of subsequent cell capture and analysis experiments.

Precise Control over the Stoichiometry, Orientation, and Modularity

The DNA nanostructure-multicomponent coding approach enables the analysis of multiproteins at the single-cell level, mainly by precisely controlling the stoichiometry, orientation, and modularity of magnetized tags and multicolor fluorescent tags, which are modified on the opposite sides of the DNA nanotubes (Figure 2a). It is well known that the photophysical

https://doi.org/10.1021/acsnano.5c18968
ACS Nano 2026, 20, 5904−5917

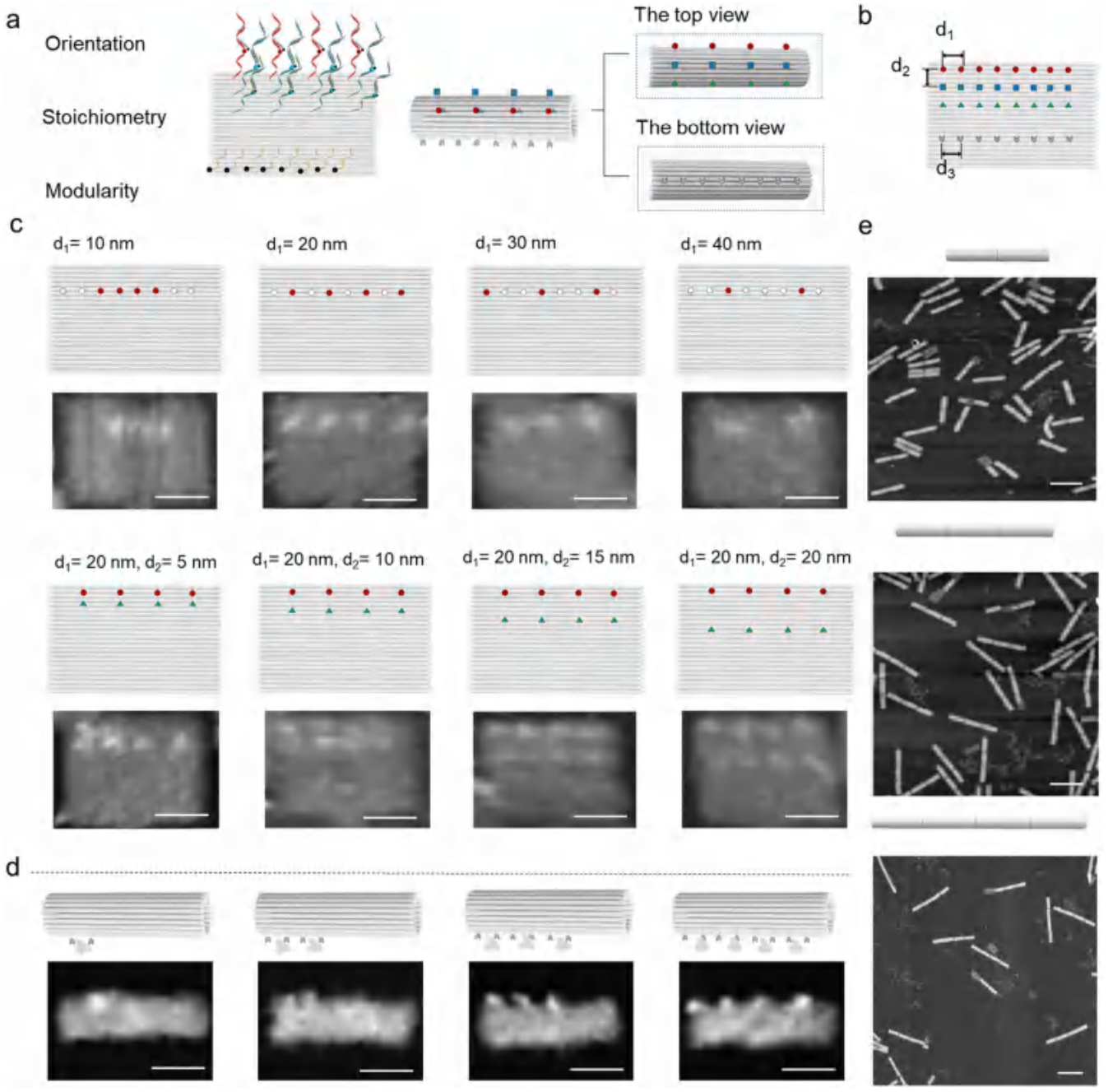

Figure 2. Programmability and addressability of DNA barcodes. (a) Schematic detailing the precise control over the stoichiometry, orientation, and modularity of the barcode components. (b) Illustration of the overall construction process of NME barcodes. (c, d) Schematic and representative AFM images of DNA nanostructures with different domains of aptamer arrays and magnetized tag arrays. Scale bars: 50 nm. (e) Schematic and representative AFM images of DNA nanotube topologies with different lengths. Scale bars: 200 nm.

properties of fluorophores on aptamer arrays are sensitive to the distance between two neighboring fluorophores. Furthermore, the different distances between aptamers determine the efficiency of binding to membrane protein receptors and the sensitivity of the multiprotein detection. Therefore, we optimized the spacing between the same and different aptamer arrays to synthesize different barcode structures. As shown in Figure 2b, a total of 24 single-stranded handles of 15 nt long are extended from the 3′ end of the strands. These sites are marked with labels and arranged in a 3 × 8 array with 10 nm row spacing and 10 nm column spacing, which serve as potential contact points for the aptamer. The docking sites can be individually programmed to include or omit the capture handle for precise control over the valency and spatial arrangement of aptamer arrays. As shown in Figures 2c and S9, we first designed and fabricated several DNA nanosheet−Apt arrays with interaptamer distances of 10 (R-Apt-10 nm), 20 (R-Apt-20 nm), 30 (R-Apt-30 nm), and 40 nm (R-Apt-40 nm). Meanwhile, they were used to optimize the barcode to obtain the optimal allocation distance for the same kind of aptamer bound to the membrane proteins. In addition, to avoid interference from photophysical signals between fluorophores on different aptamer arrays and the steric hindrance effect between different aptamers, DNA nanosheet-2 arrays with column spacings of 5 (R-2 array-5

https://doi.org/10.1021/acsnano.5c18968
ACS Nano 2026, 20, 5904−5917

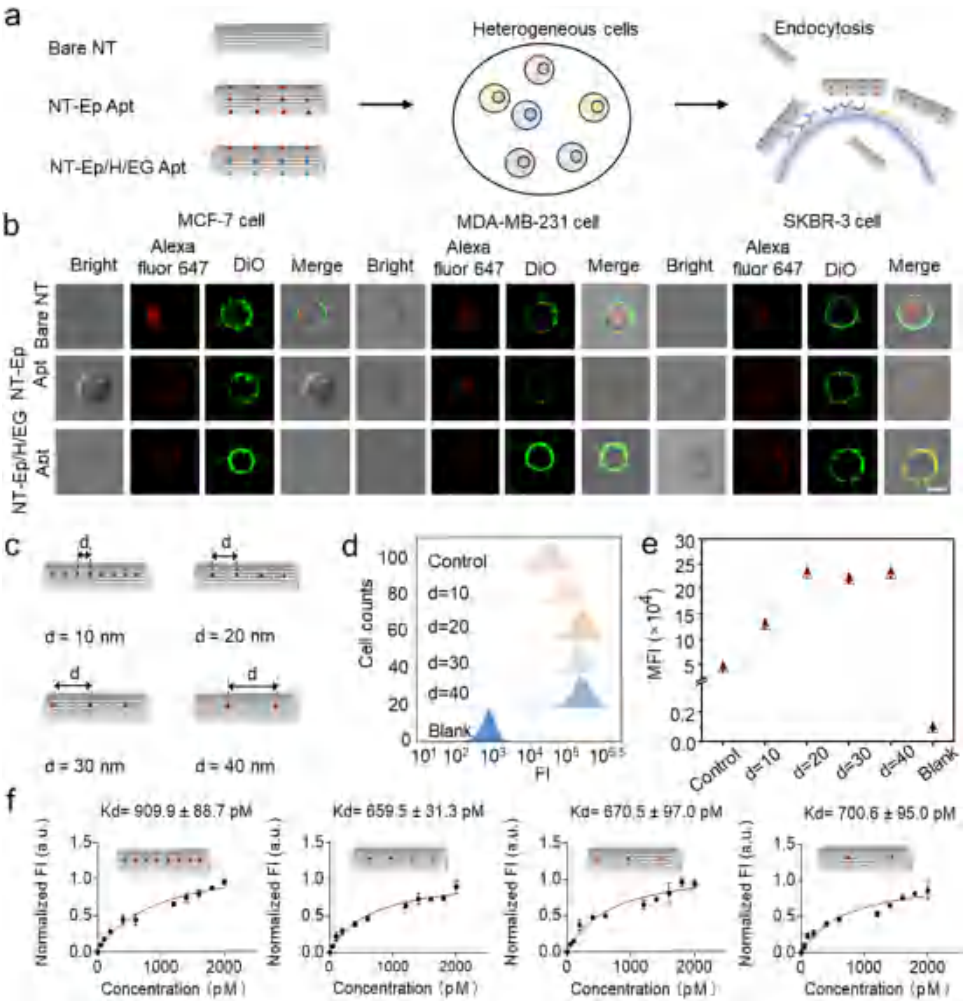

Figure 3. Targeting effect of NME barcodes on multiple protein clusters on tumor cell surfaces with high phenotypic heterogeneity. (a) Schematic illustration of the binding of bare NT, NT-Ep Apt, and NT-Ep/H/EG Apt to heterogeneous tumor cells. (b) CLSM fluorescence images showing the incubation of the three cell lines with bare NT, NT-Ep Apt, and NT-Ep/H/EG Apt. DNA nanostructures labeled with Alexa Fluor 647 (red). Scale bars: 20 μm. (c) Schematic of the different NT-Ep Apt nanostructures used to assess the effect of interaptamer spacing on the binding affinity. (d) Representative flow cytometry histograms showing the fluorescence intensity (FI) of the nanostructures in (c) bound to MCF-7 cells. (e) Quantification of the mean fluorescence intensity from flow cytometry analysis in (d). (f) Saturation binding curves for the different NT-Ep Apt nanostructures in (c) bound to MCF-7 cells, used to calculate the dissociation constant (K_d). Data are presented as mean ± s.d. from $n = 3$ independent experiments.

nm), 10 (R-2 array-10 nm), 15 (R-2 array-15 nm), and 20 nm (R-2 array-20 nm) were constructed. Although the overall morphology of the DNA nanosheets appeared similar in the overview AFM images, the success of the aptamer modification was confirmed quantitatively. As demonstrated by the line cross-sectional analysis (Figure S10, a representative analysis shown in Figure 1c,a), a significant height increase was observed specifically at the designed aptamer conjugation sites. This height profile analysis provided direct and conclusive evidence of the successful and precise modification of the aptamers.

The number of magnetic coding sites directly determines the ability to magnetically separate individual cells. Therefore, to study the relationship between them, we controlled the number of biotin-modified single-stranded DNA strands (biotin-ssDNA) on DNA nanotubes to regulate the number of magnetic coding sites, including 2, 4, 6, and 8 magnetic coding sites on a single nanotube (Figure 2d). The AFM characterization results show various numbers of SA were bound to biotin-ssDNA coding DNA nanotubes. The number of magnetic sites can be precisely programmed, ensuring low variability across the barcodes. Furthermore, DNA nanotubes with different lengths (~100, ~200, ~300, and ~400 nm) were designed to fabricate different barcodes to investigate the ability of the barcodes to target and magnetically separate heterogeneous single cells (Figures 2e, S11, and S12). These results illustrate the ability of our method to precisely control the stoichiometry, orientation, and modularity of the barcodes.

Targeting Effect of NME Barcodes to Multiple Protein Clusters on Tumor Cell Surfaces with High Phenotypic Heterogeneity

The targeting efficiency and stability of multiple proteins on tumor cell surfaces are crucial steps in the phenotypic analysis of cells with high heterogeneity. As DNA nanoprobes can be considered as nanoparticles in the field of delivery systems, they may encounter cell internalization, which could potentially impede the DNA nanoprobe binding to the proteins on the cell membrane (Figure 3a). Therefore, the distribution of our barcode on different cell lines (various EpCAM, HER2, and EGFR expression) was investigated to simulate heterogeneous

https://doi.org/10.1021/acsnano.5c18968
ACS Nano 2026, 20, 5904−5917

cells in real samples. First, the sequence length of the quencher ssDNA, which was used to quench the fluorescence intensity of the aptamer arrays, was optimized by comparing the change in the fluorescence intensity after binding with the corresponding receptor protein clusters (Figure S13). The MCF-7, SKBR-3, and MDA-MB-231 cell lines were selected as models representing Luminal A, HER2-positive, and TNBC subtypes, respectively.[45,46] The protein expression profiles identified by NME barcodes are highly consistent with the known transcriptomic classifications and genomic signatures provided by The Cancer Genome Atlas (TCGA) and the Cancer Cell Line Encyclopedia (CCLE) databases. Specifically, MCF-7 cells showed high expression of EpCAM, while SKBR-3 and MDA-MB-231 exhibited significant HER2 and EGFR overexpression, respectively, aligning with the molecular signatures of their corresponding clinical subtypes recorded in these large-scale data sets. First, the excellent biocompatibility of the barcode with MCF-7 cells was verified using the MTT assay, and the results are shown in Figure S14. After that, the targeting efficiency was investigated using a confocal laser scanning microscope (CLSM) imaging experiment. MCF-7 cells incubated with different concentrations of Alexa Fluor 647-ssDNA functionalized nanotubes for 0.5 h showed no fluorescence in the Alexa Fluor 647 channel (Figure S15). However, after incubation with Alexa Fluor 647-modified EpCAM aptamer and Alexa Fluor 647-modified EpCAM aptamer arrays functionalized DNA nanotubes (which consist of DNA nanotubes functionalized solely with the EpCAM aptamer array and lack the biotin array, termed NT-Ep Apt), CLSM images of MCF-7 cells showed significant fluorescence intensity, suggesting the cell distribution of EpCAM on MCF-7 cells (Figure S16).

Subsequently, NT-Ep Apt and Alexa fluor 647-modified EpCAM, HER2, and EGFR aptamer array-functionalized DNA nanotubes (NT-Ep/H/EG Apt) were assembled and incubated with heterogeneous breast tumor cells to evaluate their targeting efficiency and stability. As shown in Figure 3b, the CLSM imaging results showed that fluorescence signals were visible on cell membranes with high expression of EpCAM (MCF-7 and SKBR-3), indicating that NT-Ep Apt was clearly bound to membrane-targeted proteins. Instead, NT-Ep Apt was internalized by cells with low-EpCAM expression (MDA-MB-231). Furthermore, NT-Ep/H/EG Apt showed strong membrane adhesion to MCF-7, SKBR-3, and MDA-MB-231 cell lines, indicating that the three aptamer arrays on the DNA nanotubes increased the binding ability to different receptor protein clusters on the cell surface. In contrast, the bare nanotube (Bare-NT) was endocytosed by these three cell lines. These results indicate that NT-Ep/H/EG Apt can identify heterogeneous tumor cells, avoiding the loss of heterogeneous cells caused by single protein targeting.

The multivalent arrangement of aptamers greatly increases their ability to bind to different protein clusters, allowing different proteins to be recruited. To fundamentally validate that the observed targeting effect was due to specific aptamer-protein recognition, we performed rigorous internal control experiments. We constructed two types of negative control barcodes: an "Unorder" barcode, where the aptamer sequence was fully scrambled, and a "Mismatch" barcode, where critical nucleotides in the binding loop were mutated. As shown in Figure S17, in stark contrast to the strong fluorescence signals generated by the normal NME barcode, both the Unorder and Mismatch control barcodes failed to produce any detectable signal in the target cells. This result provides direct and powerful evidence that the binding function is critically dependent on the specific sequence and correctly folded three-dimensional structure of the aptamer, confirming the high specificity of our platform.

Moreover, the distance between aptamers determines the magnitude of steric hindrance, which affects their ability to target proteins. As shown in Figure 3c, to minimize steric resistance and maximize the utility of aptamers, NT-Ep Apt arrays with interaptamer distances of 10 (NT-Ep Apt-10 nm), 20 (NT-Ep Apt-20 nm), 30 (NT-Ep Apt-30 nm), and 40 nm (NT-Ep Apt-40 nm) were used to evaluate the effect of aptamer spacing on target capability (aptamer longitudinal array spacing was controlled at 10 nm and studied in the multiprotein analysis section to avoid the fluorescence resonance energy transfer (FRET) and aggregation-induced fluorescence quenching effect). The binding ability of Alexa Fluor 647-labeled EpCAM aptamer-functionalized nanotubes to MCF-7 cells was evaluated by flow cytometry. DNA nanotubes containing 1 Apt were used as a control. The results in Figure 3d3,e show that the fluorescence intensity increased as the spatial distance between the aptamers of the NT-Ep Apt increased. Moreover, NT-Ep Apt-20 nm, NT-Ep Apt-30 nm, and NT-Ep Apt-40 nm showed no significant difference in the fluorescence intensity. Furthermore, the dissociation constant (K_d) value of NT-Ep Apt-20 nm for MCF-7 cells was 659.5 ± 31.3 pM, which was relatively lower than NT-Ep Apt-10 nm (909.9 ± 88.7 pM) and comparable to that of NT-Ep Apt-30 nm (670.5 ± 97.0 pM) and NT-Ep Apt-40 nm (700.6 ± 95.0 pM) (Figure 3f). These results could be attributed to steric hindrance between the aptamers on the NT-Ep Apt-10 nanostructure, which prevents their effective binding to EpCAM at a higher valency. Conversely, excessively large spacings reduce multivalency and consequently weaken cell affinity. Therefore, considering the trade-off between steric hindrance and multivalency, 20 nm was selected as the optimal interaptamer distance. This result highlights a key design principle: optimal affinity is achieved not at the point of minimum steric hindrance, but at the "sweet spot" that best balances the relief of hindrance with the maximization of synergistic, multivalent avidity. Notably, the 20 nm construct (4 aptamers) showed significantly higher affinity than the 10 nm construct (8 aptamers), decisively demonstrating that alleviating steric hindrance via rational design is more critical than simply increasing the ligand number.

These experiments established a fundamental quantitative basis for the platform. The data in Figure 3f represent classic saturation binding experiments, where the plateauing curves confirm binding saturation and allow the calculation of an apparent K_d. This systematic study of interaptamer spacing (Figure 3c–f) also served as a direct investigation of avidity effects, quantitatively demonstrating how a rationally engineered architecture (20 nm spacing) enhanced multivalent binding. This fundamental characterization of the platform's stoichiometric binding properties validated its use for robust and relative quantification.

Multivalent Interactions of Aptamers on Barcodes Avoid EpEx Interference

Notably, it has been reported in numerous studies that the extracellular domain of EpCAM (EpEx) may undergo proteolysis and be released into the extracellular environment.[37] We believe that the distribution of receptor protein aptamer array not only improves the targeted recognition of different proteins on the surface of heterogeneous cells but also reduces

https://doi.org/10.1021/acsnano.5c18968
ACS Nano 2026, 20, 5904−5917

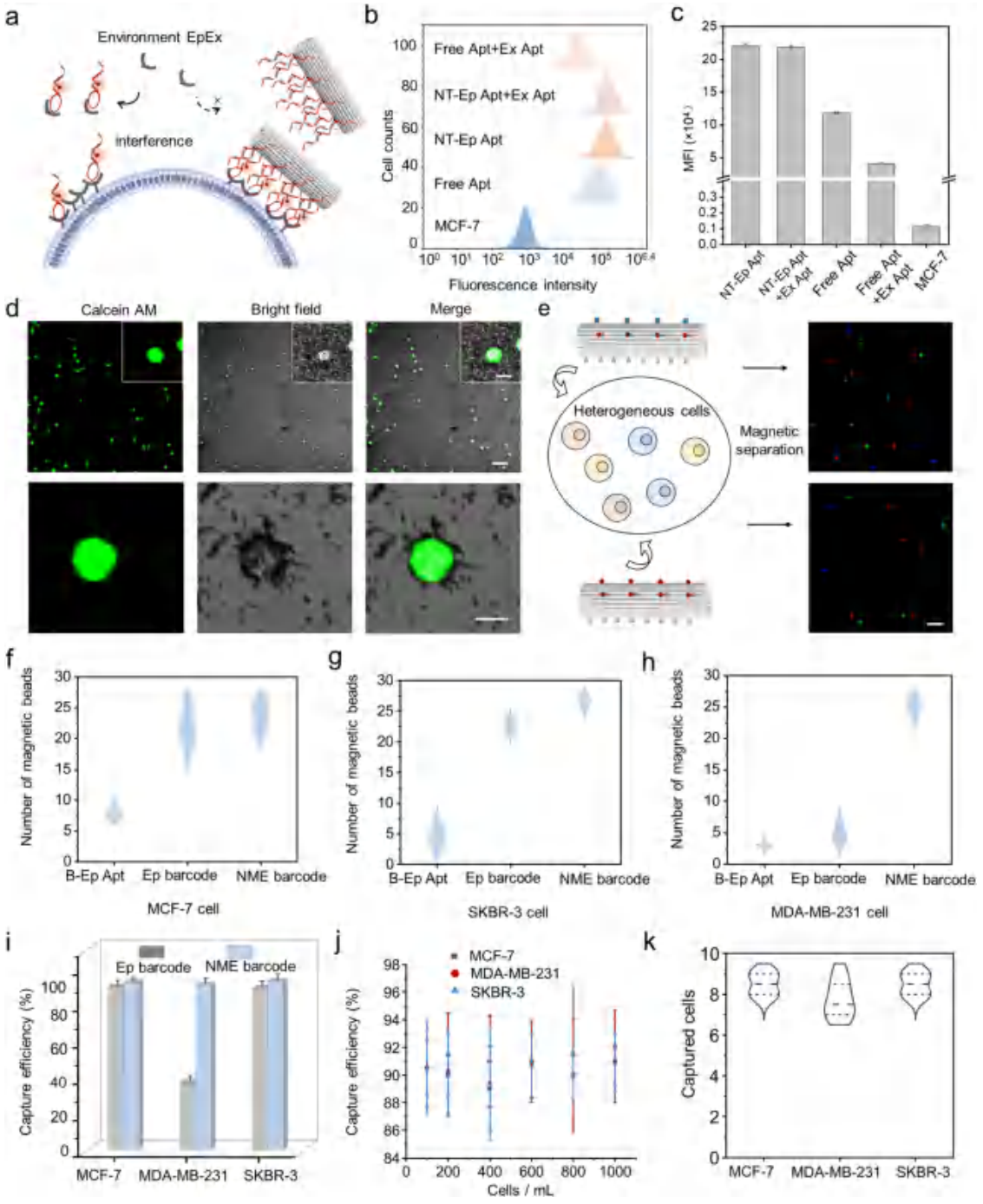

Figure 4. Multivalent interactions of aptamers on barcodes avoid EpEx interference and the separation of heterogeneous cells by the barcode. (a) The proposed mechanism of multivalent interactions improves target-binding affinity and avoids the influence of competitive binding targets, such as EpEx. (b, c) Flow cytometry analyses of free Apt and NT-Ep Apt binding to EpCAM-positive (MCF-7) cells with or without EpEx proteins in the cellular microenvironment. In (c), data are presented as mean ± s.d. from $n = 3$ independent experiments. (d) Fluorescence microscopy images of captured MCF-7 cells (labeled with AM) with conjugated magnetic beads. Insets are zoomed-in images. Scale bars: top and bottom, 100 and 20 μm, respectively; inset: 20 μm. (e) Schematic and CLSM images of the captured cell mixture composed of MCF-7 (AM-stained, green), MDA-MB-231 (Hoechst 33342-stained, blue), and SKBR-3 cells (DiL-stained, red) in equal proportions. Scale bars: 100 μm. (f-h) Quantitative analysis of magnetic beads on the surfaces of MCF-7 (f), SKBR-3 (g), and MDA-MB-231 cells (h) by particle counting after incubation with B-Ep Apt, Ep barcode, and NME barcode. (i) Comparison of capture efficiency between the Ep and NME barcodes; data represent the mean ± s.d. from $n = 3$ independent experiments. (j) Cell enrichment efficiency toward different cell lines at concentrations of 100−1000 cells/mL; data represent the mean ± s.d. from $n = 3$ independent experiments. (k) Cell enrichment at a concentration of 10 cells/mL. Violin plots show the distribution of captured cells from $n = 4$ independent experiments.

the interference of membrane protein recognition by proteins released into the extracellular microenvironment due to the hydrolysis of the extracellular domain of receptor proteins (Figure 4a). To provide more direct evidence for this improved, cluster-oriented recognition, we performed an additional quantitative cluster colocalization experiment. As shown in

https://doi.org/10.1021/acsnano.5c18968
ACS Nano 2026, 20, 5904−5917

Figure S18, our multivalent NME barcode exhibited a significantly higher Pearson's Correlation Coefficient (PCC) with antibody-defined HER2 clusters compared to the monovalent barcode control. This provided direct functional imaging evidence that our multivalent design confers preferential targeting of protein clusters. After that, a recombinant human EpEx protein was added to the extracellular environment of MCF-7 cells, and the binding abilities of Ep Apt and NT-Ep Apt to membrane proteins were investigated. As shown by the flow cytometry analysis in Figure 4b4,c, the binding ability of NT-Ep Apt to MCF-7 cells was obviously higher than that of Ep Apt, indicating that the array arrangement of NT-Ep Apt had a stronger binding ability with the EpCAM clusters on the cell membrane. The presence of EpEx obviously reduced the binding ability of Ep Apt, while EpEx had no significant effect on NT-Ep Apt, indicating that the polyvalent binding between the aptamer array and cells could largely resist EpEx, which was consistent with previous research.[47]

Separation of Heterogeneous Cells

After validating the targeting efficiency and stability of the NME barcodes in multiple membrane protein clusters, we further investigated the ability of the NME barcode to capture heterogeneous breast cancer cells. First, MCF-7 cells were used to verify the feasibility of the magnetic separation of the NME barcode. Specifically, MCF-7 cells labeled with calcein AM dye (a cell-permeable dye, green) were incubated with NME barcodes and subjected to magnetic isolation. As shown in Figure 4d, many magnetic beads were coupled to the membrane of MCF-7 cells after magnetic separation by the NME barcodes, which demonstrated the ability of NME barcodes to isolate MCF-7 cells. To further study the capture capacity of the NME barcode on heterogeneous cells with different expression levels of EpCAM, HER2, and EGFR, we compared the capture efficiency of the NME barcode with a single aptamer EpCAM array-encoded barcode (a single-target capture control functionalized with only the EpCAM aptamer array and biotin array, termed as Ep barcode) on MCF-7 cells, MDA-MB-231 cells, and SKBR-3 cells. The same number of MCF-7 cells, MDA-MB-231 cells, and SKBR-3 cells were prestained with different dyes, calcein AM, Hoechst 33342 (a live nuclear marker dye), and DiL (cell-membrane red fluorescent probe), and then incubated with the NME barcode and Ep barcode for magnetic separation. As shown in Figures 4e and S19, the NME barcode showed more accurate cell capture than the Ep barcode, and the number of isolated cells was close to 1:1:1. Conversely, the cells captured by the Ep barcode showed an unbalanced proportion, with a larger proportion of high-EpCAM cells (MCF-7 and SKBR-3 cells). Furthermore, representative fluorescence microscopy images of the biotinylated EpCAM aptamer (B-Ep Apt), Ep barcode, and NME barcode after incubation with MCF-7, SKBR-3, and MDA-MB-231 cells also indicated the strong magnetic separation ability of the NME barcode (Figures 4f–h and S20).

To demonstrate the advantages of our multiantigen recognition strategy, we first compared the capture efficiency of the multitarget NME barcode against a single-target "Ep barcode" (targeting only EpCAM). The same number of MCF-7 cells, SKBR-3 cells, and MDA-MB-231 cells were mixed with 1×10^6 mononuclear cells/mL to simulate clinical samples and incubated with the NME and Ep barcodes, followed by magnetic separation. The captured cells were observed and counted by using fluorescence microscopy. As shown in Figure 4i, for high-EpCAM cells (MCF-7 and SKBR-3), both barcodes performed well. Critically, for low-EpCAM MDA-MB-231 cells, the multitarget NME barcode achieved a capture efficiency of 90.5% ± 3.0%, dramatically outperforming the Ep barcode (37.0% ± 3.0%). This result decisively proved that multitarget design is essential for effectively capturing phenotypically heterogeneous tumor cells. Furthermore, we evaluated the NME barcode's performance across a range of clinically relevant concentrations, consistently achieving recovery rates of around 90% (Figure 4j). The platform's sensitivity was confirmed with an average enrichment rate of over 70% for samples containing just 10 cells/mL, establishing an effective limit of detection (LOD) for rare cell analysis (Figure 4k).

To further evaluate the practical performance, we conducted a direct head-to-head benchmark against standard, commercially available CD326 (EpCAM) immunomagnetic bead-based immunoisolation. In this experiment, 100 tumor cells were spiked into a background of 1×10^6 healthy donor mononuclear cells. The results, summarized in Table S1, point to two key advantages of our platform. First, for low-EpCAM cells, the NME barcode recovery rate (90.5% ± 3.0%) was over 2.5 times higher than that of the commercial beads (35.7% ± 8.9%). Second, our method yielded a captured product with over 3-fold higher purity (32.2% vs 10.3%), a direct result of capturing significantly fewer background white blood cells (~200 vs ~733). This benchmark provides strong evidence that the NME barcode platform offers substantial advantages in terms of yield and purity over standard immunoisolation methods.

Furthermore, the captured cells (SKBR-3 cells) were identified with immunocytochemistry. The white blood cells (WBCs) were used as control cells. The barcode with EpCAM/HER2 aptamer array for labeling HER2 and EpCAM, allophycocyanin (APC)-antiCD45 for labeling CD45 (a marker of WBCs). The results in Figure S21 indicate that CD45-/HER2+ cells were identified as tumor cells. To achieve cell release, we further used a short DNA sequence (DNA for release, whose sequence is listed in the Supporting Information) to break the bridge between the cell membrane and magnetic beads, which was built by the complementary pairing of DNA bases. As shown in Figure S22a, the release efficiencies for all three tested cell lines (MCF-7, MDA-MB-231, and SKBR-3) were greater than 92%. As shown in Figures S22b and S23, the cells after capture and release had good activity for further proliferation. Therefore, the NME barcode has an excellent ability to separate heterogeneous cells and can support downstream analysis.

Profiling Multiprotein for Heterogeneous Cell Classification

The directional assembly of magnetized tag arrays and multicolor fluorescence aptamer arrays of NME barcodes was designed for the efficient targeting of breast cancer cells with a high degree of phenotypic heterogeneity and profiling of multiplex protein clusters on their surface. Quantitative benchmarking (Table S2) highlights the NME platform's superior sensitivity and molecular resolution compared to the high-input CITE-seq and CyTOF workflows. Crucially, by prioritizing biocompatibility, our workflow preserves high postanalysis viability, establishing a unique niche for the functional analysis of rare cells. After that, we evaluated the ability of the barcode for simultaneous analysis of the cell surface multiprotein and cell classification.

Specifically, a known number of MCF-7, SKBR-3, and MDA-MB-231 cells were mixed with 1×10^6 mononuclear cells from the whole blood of a healthy person to simulate clinical samples

https://doi.org/10.1021/acsnano.5c18968
ACS Nano 2026, 20, 5904−5917

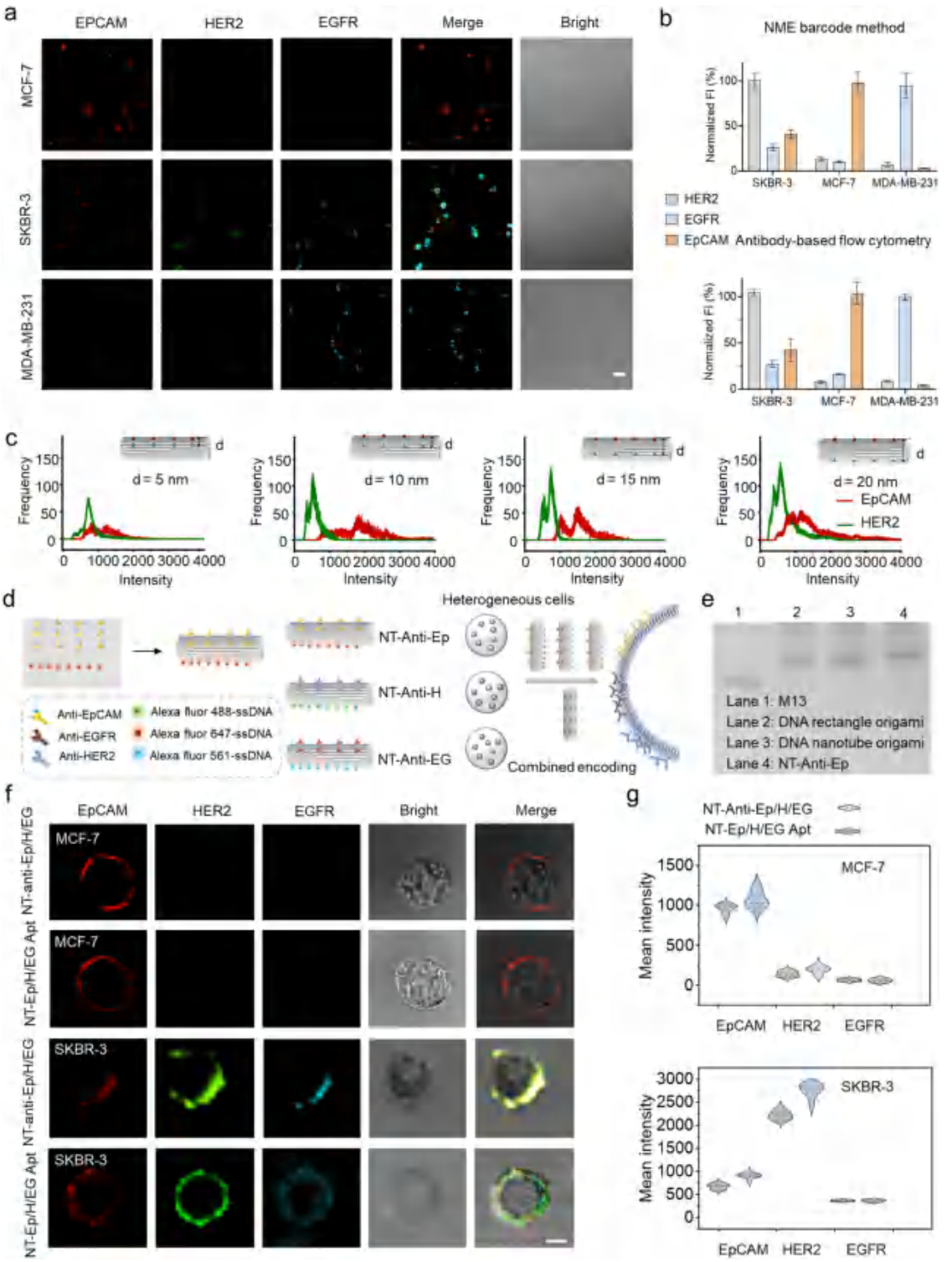

Figure 5. Heterogeneous cell classification at the single-cell level. (a) Fluorescence microscopy images showing multiprotein profiling of MCF-7, SKBR-3, and MDA-MB-231 cells. Scale bars: 100 μm. (b) Quantitative validation of protein expression levels (EpCAM, HER2, EGFR) via antibody-based flow cytometry, showing high consistency with the NME barcode method; data represent the mean ± s.d. from n = 3 independent experiments. (c) Analysis of fluorescence signal interference by varying the row pitch (5, 10, 15, and 20 nm) between the aptamer arrays. (d) Schematic illustration of the construction of antibody-encoded barcodes. (e) 1% agarose gel electrophoresis, confirming the assembly of antibody-encoded barcodes. (f) Comparative fluorescence imaging of MCF-7 and SKBR-3 cells using aptamer-encoded barcodes (NT-Ep/H/EG Apt) versus antibody-encoded barcodes. Scale bars: 10 μm. (g) Quantitative comparison of fluorescence intensity between the two methods described in (f). Violin plots show the distribution of the captured cells (n = 10).

and then magnetically isolated for subsequent profiling of the multimembrane protein. As shown in the fluorescence microscopy images in Figure 5a, the cell lines displayed distinct protein expression profiles. As previously described, the cell lines displayed distinct, clinically relevant protein expression profiles (EpCAM-high for MCF-7, HER2-high for SKBR-3, and EGFR-

https://doi.org/10.1021/acsnano.5c18968
ACS Nano 2026, 20, 5904−5917

high for MDA-MB-231), which were accurately resolved by our NME barcodes. To quantitatively validate these observations, we compared our NME barcode method with the gold-standard technique, antibody-based flow cytometry, and the analysis results are presented in Figure 5b. We analyzed three proteins (EpCAM, HER2, and EGFR) in three core cell lines (MCF-7, SKBR-3, and MDA-MB-231). The results indicated that the protein expression patterns and relative expression levels measured by both methods were highly consistent, providing a robust, population-level orthogonal validation for our method's quantitative accuracy, which was consistent with previous literature reports.[48,49] This orthogonal validation provided robust, population-level confirmation of the quantitative accuracy of the NME barcode strategy for analyzing multiple biomarkers. Furthermore, precise regulation of coding can greatly improve the feasibility and reliability of barcodes for the analysis of a wide range of cellular biomarkers.

To directly address whether the multivalent NME barcode could induce artificial receptor activation, we performed functional assays for all three target receptors. First, we used Western blotting to measure the phosphorylation of the key activation sites on EGFR (pY1068) and HER2 (pY1248). As shown in Figure S24a,b, the results clearly showed no significant increase in phosphorylation in the barcode-treated cells compared to the untreated controls. Second, since EpCAM signals via a different mechanism, we used qPCR to measure the expression of its downstream target genes, cMyc and cyclin D1. The results also showed no significant changes in mRNA levels (Figure S24c). This comprehensive functional data provided strong evidence that our platform binds to its targets with high affinity without causing unwanted cross-linking or altering their native signaling states.

In our platform, the signal channel resolution is determined by the spectral properties of the chosen fluorophores. We selected Alexa Fluors 488, 561, and 647, which are spectrally well-separated commercial dyes that can be effectively distinguished using standard microscopy filter sets. To further avoid the interference of the photophysical properties of fluorophores on the aptamer arrays in the multicolor fluorescence analysis, we assembled DNA nanotubes with EpCAM and HER2 targeting aptamer arrays (labeled by Alexa Fluor 647 and Alexa Fluor 488, respectively).[50,51] By controlling the distance between different DNA aptamer arrays, we assembled the DNA nanotube nanostructure-2 arrays with row pitches of 5 (NT-2 arrays-5 nm), 10 (NT-2 arrays-10 nm), 15 (NT-2 arrays-15 nm), and 20 nm (NT-2 arrays-20 nm). After that, different DNA nanotube-2 arrays were then used to target EpCAM and HER2 on the cell membrane of MDA-MB-453 cells, which have been reported to express these two membrane proteins.[40,41] As shown in Figures 5c and S25, the fluorescence intensities in the channels of Alexa Fluor 647 and Alexa Fluor 488 were higher in the NT-2 arrays-10 nm group than in the NT-2 arrays-5 nm group. Crucially, the fluorescence intensity reached a stable plateau at spacings of 10, 15, and 20 nm, demonstrating that an interarray distance of 10 nm was sufficient to completely eliminate FRET-based signal crosstalk, thus ensuring the fidelity of the multiplexed analysis. To quantitatively assess the batch-to-batch consistency of our platform, we prepared three independent batches of NME barcodes and measured the fluorescence intensities of each of the three fluorophores (Alexa Fluors 488, 561, and 647), which corresponded to the HER2, EGFR, and EpCAM targeting modules, respectively. The fluorescence intensity measurements showed a Relative Standard Deviation (RSD) of less than 4% between batches, confirming the high coupling efficiency, low yield variation, and overall high reproducibility of our fabrication process (Figure S26).

A key aspect of our platform's design is the ∼100 nm length of the DNA nanotube. It is important to clarify that this structure is not intended to fit 'inside' a smaller receptor cluster but rather to act as a "spanning scaffold" that lies parallel to the cell membrane, enabling multivalent interactions with one or more adjacent clusters. This size was not an arbitrary choice but was the result of a systematic optimization study, which is presented in the Supporting Information. As shown in Figures S27 and S28, the 100−200 nm length was found to provide the optimal balance between high capture efficiency and maximum fluorescence signal intensity. Paired with functional data demonstrating its biological inertness, this rationally optimized design confirms the platform's suitability for live-cell analysis.

To ensure optimal performance under physiological conditions, we systematically investigated the effects of temperature and critical ion concentrations on the protein analysis signal. The results demonstrated that the NME barcode achieved the maximum detection performance for all protein targets at a physiological temperature of 37 °C and Mg^{2+} concentration of 10 mM (Figure S29). These optimized conditions were used in all subsequent experiments.

To further verify the compatibility and generality of the aptamer-encoded barcodes with traditional antigen−antibody binding immunoassays, we replaced the fluorophore-labeled aptamer sequences in the barcode assembly process with the anti-ssDNA conjugates, so that the proteins on the surface of the cell membrane could bind to the corresponding antibodies. First, as shown in Figure 5d, the DNA nanotubes encoded by the EpCAM, HER2, and EGFR antibodies (NT-anti-Ep, NT-anti-H, NT-anti-EG) were prepared. Anti-ssDNA conjugates were prepared using the sulfosuccinimidyl-4-(*N*-maleimidomethyl)-cyclohexane-1-carboxylate (SMCC) cross-linking method, and further assembled on DNA origami nanostructures. Antibody labeling barcodes (antibarcodes) were characterized by agarose gel electrophoresis. As shown in the agarose gel electrophoresis analysis results in Figure 5e, after antibody assembly, the gel electrophoresis band had a larger molecular weight than both the bare DNA rectangle origami nanostructure and the DNA nanotube nanostructure, further indicating the successful assembly of the antibody labeling barcode. The ability of heterogeneous cell classification of aptamer-encoded barcodes with antibarcode was investigated by fluorescence analysis. As shown in Figure 5f, the fluorescence imaging results for both barcode types were highly consistent. For MCF-7 cells, both methods indicated high expression of EpCAM. Similarly, for SKBR-3 cells, both methods showed high HER2 expression, accompanied by low expression of EpCAM and EGFR. Moreover, the total fluorescence intensity values of each protein expression at the single-cell level also showed that the results of the two methods were consistent (Figure 5g). This proved that the NME barcode has great potential for the simultaneous analysis of multiple proteins, demonstrating its compatibility with antibody-based recognition, even if the corresponding aptamers are not selected for all targets.

Although the 3-plex panel demonstrated here served to validate the platform's core workflow, scalability is a key consideration for future applications. A practical path to higher multiplexing involves expanding to a 6−8 plex panel by incorporating additional spectrally distinct fluorophores coupled with established spectral unmixing algorithms. How-

https://doi.org/10.1021/acsnano.5c18968
ACS Nano 2026, 20, 5904−5917

ever, achieving the theoretical multiplexing capacity of the NME platform requires addressing several biophysical constraints. First, as the number of targets increases, fluorescence bleed-through between adjacent spectral channels becomes the primary limiting factor, necessitating the use of advanced spectral unmixing and narrow-emission fluorophores. Second, higher-order multiplexing requires rigorous optimization of barcode sequence orthogonality to prevent nonspecific cross-hybridization between the capture handles and aptamer sequences. Lastly, the precise interaptamer spacing balances steric hindrance and potential interference to maintain a high binding affinity. We acknowledge that optical-fluorescence-based methods face inherent limitations in channel capacity compared to the fundamentally different physics of mass cytometry. Therefore, the unique value of the NME platform lies not in competing on parameter count but in combining moderate-plex profiling with its nondestructive cell isolation and culture capabilities. This enables a direct link between a cell's molecular phenotype and its subsequent biological function, a crucial gap that high-plex terminal-analysis methods like CyTOF do not address.

CONCLUSIONS

In conclusion, we have developed a multicomponent-encoded method that leverages the structural programmability and addressability of DNA origami nanostructures. The designed NME barcode could achieve efficient targeting and profiling of multiplex protein clusters on the surface of tumor cells with a high degree of phenotypic heterogeneity, allowing for the simultaneous separation of heterogeneous cells and multicolor fluorescence combination encoding of phenotypes. Compared with traditional DNA-based synthetic barcodes, modular NME barcodes overcome multiplexing limitations caused by the lack of precise control over stoichiometry, orientation, and modularity. By further trapping individual cells, we show that the molecular subtypes of breast cancer can be accurately classified by a single-cell fluorescence coding signature. Moreover, the fine-tuned design of magnetized tag arrays and multicolor fluorescent aptamer arrays significantly enhances the feasibility and reliability of barcodes for analyzing diverse cellular biomarkers, enabling more complex and precise molecular typing tasks. This strategy provided a versatile platform for multiplex bioassays, including cell sorting, proteomic profiling, and genomic analysis, thereby advancing the frontiers of precision medicine. Although this study successfully demonstrated proof-of-concept using established cell line models, future studies should focus on correlating the findings with clinical metadata and established pathological methods, such as immunohistochemistry (IHC), to fully validate its clinical utility.

METHODS

Preparation of DNA Origami Templates and NME Barcodes

The DNA origami templates were prepared by a one-pot process.[1] 100 nM of the M13mp18 DNA scaffold strand (5 μL) was mixed with 200 nM of DNA staple strands (10 μL) and 25 nM of DNA foothold strands in 1 × TAE/Mg^{2+} buffer (Tris, 40 mM; acetic acid, 20 mM; EDTA, 2 mM; magnesium acetate, 12.5 mM; pH 8.0). Annealing was performed from 95 °C to room temperature in 2 h to obtain the DNA origami templates. Finally, the prepared DNA origami templates were purified four times with 100 kDa (Merck Millipore) centrifuge filters to remove excess DNA strands and then redispersed in 1 × TAE/Mg^{2+} buffer. The concentration of the DNA origami templates was quantified by ultraviolet spectroscopy. The barcodes were obtained by mixing the DNA origami templates, DNA aptamers, and biotin-functionalized DNA strands at a concentration ratio of 1:5:5 and naturally annealed from 55 °C to room temperature.

Gel Electrophoresis

All DNA nanostructures were subjected to 1% agarose gel electrophoresis at 60 V for 90 min in an ice water bath. Gels were prepared with 1× TBE buffer containing 10 mM $MgCl_2$ and left to solidify at room temperature for at least 1 h before use. GelRed (41,003, Biotium) was added to the agarose gels for imaging under UV light, according to the manufacturer's instructions. For fluorescence imaging, samples were loaded onto gels without GelRed in a dye-free loading buffer (30% glycerin, 6×).

Atomic Force Microscopy Imaging

The morphologies of the rectangular and tubular DNA origami templates, NME barcodes, and other DNA nanostructures were determined by AFM (SPM Multimode with Nanoscope V controller, Bruker). For sample preparation, a 5 μL drop of the sample (5 nM) was deposited onto a freshly cleaved mica surface for 2 min, followed by the addition of 60 μL of 1× TAE buffer containing 10 mM $MgCl_2$ for liquid imaging. All images were acquired in Peak Force Tapping mode by using a ScanAsyst-Fluid+ (Bruker) probe. The scanning parameters were set to a scan rate of 1.0 Hz and a resolution of 384 × 384 pixels. Postimaging processing, including plane correction and height profile extraction, was performed by using the NanoScope Analysis software.

Cell Culture

Human breast cancer cell lines (MCF-7, MDA-MB-231, and SKBR-3) were cultured in Dulbecco's modified Eagle's medium (DMEM, Gibco) supplemented with 10% fetal bovine serum (FBS, Gibco) and 1% penicillin-streptomycin (Gibco) in a 37 °C incubator with 5% CO_2.

Cell Viability Assay

MCF-7 cells were precultured in 96-well plates (200 μL, 1 × 10^4 cells·$well^{-1}$) at 37 °C for 24 h. After removing the original medium, the cells were incubated with NME barcode, bare NT, and Ep barcode (1 nM, 5 nM, 10 nM) for 12 h. Then, 200 μL of MTT solution (0.5 mg/mL in PBS) was added to the above samples and incubated for 4 h to form formazan. After removing the excess MTT, 150 μL of dimethyl sulfoxide was added. Finally, the absorbance at 490 nm was measured with a microplate reader.

Cellular Distribution Imaging

MCF-7, MDA-MB-231, and SKBR-3 cells were first seeded at a density of 5 × 10^4 cells/mL in 35 mm glass-bottomed culture dishes. After 12 h, the cells were washed with PBS three times and then incubated with serum-free DMEM containing Alexa Fluor 647-labeled bare NT, NT-Ep Apt, and NT-Ep/H/EG Apt for 4 h at 37 °C. Free DNA nanostructures were then washed with BB buffer (1× PBS, 5 mM $MgCl_2$, pH 7.4) three times. Subsequently, the cell membrane was stained with 20 μg/mL DiO (Beyotime) for 15 min, followed by washing three times with PBS. The cellular distribution of the DNA nanosynapse was imaged by a confocal microscope (FV 3000 Olympus).

Flow Cytometric Analysis

MCF-7 cells were cultured to approximately 70% confluency, detached with a nonenzymatic cell dissociation buffer, and washed 3 times with ice-cold PBS. 2.5 × 10^5 cells were incubated with 250 nM Alexa Fluor 647-labeled EpCAM Apt or NT-Ep Apt in binding buffers. Samples in the experimental group also contained 2.5 μg/mL human recombinant EpCAM EpEx protein. After incubation for 40 min, the cells were pelleted (500 g, 5 min, 4 °C), washed three times, and then subjected to flow cytometry.

Cell Capture and Release

MCF-7, MDA-MB-231, and SKBR-3 cells were stained with calcin AM dye, Hoechst 33342, and DiL, respectively, in PBS at 4 °C for 30 min. After three wash cycles with PBS, the cells were resuspended in PBS, and the cell density was measured by a cell counter. A certain number of

https://doi.org/10.1021/acsnano.5c18968
ACS Nano 2026, 20, 5904−5917

labeled cells or cell mixtures were spiked with 1×10^6 mononuclear cells/mL and incubated with 5 nM Ep and NME barcodes, respectively, in BB buffer at 4 °C for 30 min with a final volume of 200 μL. 5 μL of streptavidin beads (5 μL, 10 mg/mL, 1 μm) was then added, and incubated for another 30 min. After magnetic separation, the cells were washed three times with BB buffer and resuspended in PBS. The captured cells were then transferred to a 32-well plate and counted by a fluorescence microscope (IX83, Olympus). The capture efficiency is defined as the percentage of captured cells vs the total number of cells initially spiked. Finally, the mononuclear cells were suspended in 1 mL of PBS for further use. A known number of these three kinds of cells were mixed with 1×10^6 mononuclear cells from the whole blood of a healthy person to simulate clinical samples and then magnetically isolated for subsequent profiling of the multimembrane protein by fluorescence microscopy. The isolated cells were stained with Anti-Human CD45 to count the number of nonspecific WBCs. To achieve cell release, the captured cells were resuspended in DMEM, containing 10% FBS, and treated with 100 nM released DNA strands, which could replace the biotin single-strand DNA at room temperature for 30 min. Next, the mixture was pipetted thoroughly to maximize cell release, followed by the magnetic separation of the beads. The released cells were then transferred to a 32-well plate and counted by a fluorescence microscope. The cell release efficiency was calculated as the percentage of released cells of the captured cells.

Profiling Multiprotein of Heterogeneous Tumor Cells

The captured cells were imaged by CLSM and TIRFM. With the NIS-Elements AR Analysis software, fluorescence intensities of single cells at excitation wavelengths of 647, 488, and 561 nm were outputted conveniently and efficiently for profiling EpCAM, HER2, and EGFR, respectively. The fluorescence intensity data of hundreds of cells were obtained using a Microplate analysis system (Biotek CBM).

Preparation of Antibarcode

Antibody-single-stranded DNA (anti-ssDNA) conjugates used for the construction of the antibarcodes were prepared using an established protocol involving a bifunctional cross-linker.[2] This method utilizes thiol-maleimide chemistry to form a stable covalent bond between the antibody and DNA via the cross-linker sulfosuccinimidyl-4-(N-maleimidomethyl) cyclohexane-1-carboxylate (sulfo-SMCC). The process consisted of several key steps: The antibody was first activated by reacting it with a 5-fold molar excess of sulfo-SMCC in PBS at 4 °C for 3 h. One end of the sulfo-SMCC molecule reacts with amine groups on the antibody. After the reaction, unreacted sulfo-SMCC was completely removed from the activated antibody using an Ultra-0.5 mL centrifugal filter with three successive washing and centrifugation steps (3 min at 5,534 g). The purified antibody was then mixed with a 5-fold molar excess of thiolated poly-T DNA strand and incubated overnight. The maleimide group on the other end of the sulfo-SMCC specifically reacts with the thiol group on the DNA. Finally, the resulting antibody–DNA conjugates were purified from excess unreacted DNA using a centrifugal filter (10 min at 3000*g*) to yield the final product.

Statistical Analysis

All quantitative values are presented as mean ± standard deviation. Statistical analyses were carried out using the GraphPad Prism software.

Human Cell Samples

Human peripheral blood mononuclear cells were obtained from Milecell Biological Science & Technology Co., Ltd. (Shanghai, China). The study protocol and use of human-derived samples were reviewed and approved by the Institutional Review Board of Shanghai Liquan Hospital (Ethics Approval Number: Z-ZJMS-21-10-001). All healthy donors provided written informed consent prior to the sample collection. All human-derived materials were handled in a deidentified manner to protect donor privacy and were used strictly for research purposes.

■ ASSOCIATED CONTENT

Supporting Information

The Supporting Information is available free of charge at https://pubs.acs.org/doi/10.1021/acsnano.5c18968.

Experimental materials, AFM, and agarose gel images; DNA origami stability detection; fluorescence spectra response; cytotoxicity assays; fluorescence microscopy images; immunofluorescence staining images; oligonucleotide sequences used; and additional references (PDF)

■ AUTHOR INFORMATION

Corresponding Author

Jie Chao − *State Key Laboratory for Flexible Electronics (LoFE), Nanjing University of Posts and Telecommunications, Nanjing 210023, China; Jiangsu Key Laboratory of Smart Biomaterials and Theranostic Technology and College of Materials Science and Engineering, Nanjing University of Posts and Telecommunications, Nanjing 210023, China;* orcid.org/0000-0003-1030-9944; Email: iamjchao@njupt.edu.cn

Authors

Meirong Cui − *State Key Laboratory for Flexible Electronics (LoFE), Nanjing University of Posts and Telecommunications, Nanjing 210023, China; Jiangsu Key Laboratory of Smart Biomaterials and Theranostic Technology and College of Materials Science and Engineering, Nanjing University of Posts and Telecommunications, Nanjing 210023, China*

Chenxu Hu − *State Key Laboratory for Flexible Electronics (LoFE), Nanjing University of Posts and Telecommunications, Nanjing 210023, China; Jiangsu Key Laboratory of Smart Biomaterials and Theranostic Technology and College of Materials Science and Engineering, Nanjing University of Posts and Telecommunications, Nanjing 210023, China*

Jiahan Dong − *State Key Laboratory for Flexible Electronics (LoFE), Nanjing University of Posts and Telecommunications, Nanjing 210023, China; Jiangsu Key Laboratory of Smart Biomaterials and Theranostic Technology and College of Materials Science and Engineering, Nanjing University of Posts and Telecommunications, Nanjing 210023, China*

Yiyu Cheng − *State Key Laboratory for Flexible Electronics (LoFE), Nanjing University of Posts and Telecommunications, Nanjing 210023, China; Jiangsu Key Laboratory of Smart Biomaterials and Theranostic Technology and College of Materials Science and Engineering, Nanjing University of Posts and Telecommunications, Nanjing 210023, China*

Bicheng Sun − *State Key Laboratory for Flexible Electronics (LoFE), Nanjing University of Posts and Telecommunications, Nanjing 210023, China; Jiangsu Key Laboratory of Smart Biomaterials and Theranostic Technology and College of Materials Science and Engineering, Nanjing University of Posts and Telecommunications, Nanjing 210023, China*

Chunhai Fan − *School of Chemistry and Chemical Engineering, Shanghai Jiao Tong University, Shanghai 200240, China; Frontiers Science Center for Transformative Molecules and National Center for Translational Medicine, Shanghai Jiao Tong University, Shanghai 200240, China; Zhangjiang Institute for Advanced Study, Shanghai Jiao Tong University, Shanghai 201203, China;* orcid.org/0000-0002-7171-7338

https://doi.org/10.1021/acsnano.5c18968
ACS Nano 2026, 20, 5904−5917

Lianhui Wang − *State Key Laboratory for Flexible Electronics (LoFE), Nanjing University of Posts and Telecommunications, Nanjing 210023, China; Jiangsu Key Laboratory of Smart Biomaterials and Theranostic Technology and College of Materials Science and Engineering, Nanjing University of Posts and Telecommunications, Nanjing 210023, China;* orcid.org/0000-0001-9030-9172

Complete contact information is available at: https://pubs.acs.org/10.1021/acsnano.5c18968

Author Contributions

M.R.C. conceived and designed the study, and designed the sequences of the DNA scaffolds. M.R.C., C.X.H., and J.H.D. performed the AFM experiments. M.R.C. and Y.Y.C. performed agarose gel electrophoresis. M.R.C., C.X.H., and J.H.D. performed cell capture and release experiments. M.R.C., C.X.H., and B.C.S. performed fluorescence microscopy experiments. C.X.H. performed data analysis. M.R.C., J.C., C.H.F., and L.H. Wang led the manuscript preparation.

Notes

The authors declare no competing financial interest.

■ ACKNOWLEDGMENTS

This work was supported by the National Key Research and Development Program of China (2024YFA1209402), the National Natural Science Foundation of China (22274081, 62201288, 62288102), and the Leading-edge Technology Program of Jiangsu Natural Science Foundation (BK20212012).

■ REFERENCES

(1) Thomasian, N. M.; Kamel, I. R.; Bai, H. X. Machine Intelligence in Non-Invasive Endocrine Cancer Diagnostics. *Nat. Rev. Endocrinol.* **2022**, *18*, 81−95.

(2) Nassiri, F.; Chakravarthy, A.; Feng, S. R.; Shen, S. Y.; Nejad, R.; Zuccato, J. A.; Voisin, M. R.; Patil, V.; Horbinski, C.; Aldape, K.; Zadeh, G.; De Carvalho, D. D. Detection and Discrimination of Intracranial Tumors Using Plasma Cell-Free DNA Methylomes. *Nat. Med.* **2020**, *26*, 1044−1047.

(3) Nam, A. S.; Chaligne, R.; Landau, D. A. Integrating Genetic and Non-Genetic Determinants of Cancer Evolution by Single-Cell Multi-Omics. *Nat. Rev. Genet.* **2021**, *22*, 3−18.

(4) Landegren, U.; Al-Amin, R. A.; Björkesten, J. A Myopic Perspective on the Future of Protein Diagnostics. *New Biotechnol.* **2018**, *45*, 14−18.

(5) Borrebaeck, C. A. K. Precision Diagnostics: Moving Towards Protein Biomarker Signatures of Clinical Utility in Cancer. *Nat. Rev. Cancer* **2017**, *17*, 199−204.

(6) Ambrosetti, E.; Bernardinelli, G.; Hoffecker, I. T.; Hartmanis, L.; Kiriako, G.; de Marco, A.; Sandberg, R.; Högberg, B.; Teixeira, A. I. A DNA-Nanoassembly-Based Approach to Map Membrane Protein Nanoenvironments. *Nat. Nanotechnol.* **2021**, *16*, 85−95.

(7) Wang, L. P.; Liang, H.; Sun, J.; Liu, Y. C.; Li, J. Y.; Li, J. Y.; Li, J.; Yang, H. H. A. Bispecific Aptamer Induced Artificial Protein-Pairing: A Strategy for Selective Inhibition of Receptor Function. *J. Am. Chem. Soc.* **2019**, *141*, 12673−12681.

(8) Klein, A. M.; Mazutis, L.; Akartuna, I.; Tallapragada, N.; Veres, A.; Li, V.; Peshkin, L.; Weitz, D. A.; Kirschner, M. W. Droplet Barcoding for Single-Cell Transcriptomics Applied to Embryonic Stem Cells. *Cell* **2015**, *161*, 1187−1201.

(9) Garzoni, M.; Okuro, K.; Ishii, N.; Aida, T.; Pavan, G. M. Structure and Shape Effects of Molecular Glue on Supramolecular Tubulin Assemblies. *ACS Nano* **2014**, *8*, 904−914.

(10) Lee, J.; Bisso, P. W.; Srinivas, R. L.; Kim, J. J.; Swiston, A. J.; Doyle, P. S. Universal Process-Inert Encoding Architecture for Polymer Microparticles. *Nat. Mater.* **2014**, *13*, 524−529.

(11) Jones, M. R.; Seeman, N. C.; Mirkin, C. A. Programmable Materials and the Nature of the DNA Bond. *Science* **2015**, *347*, No. 1260901.

(12) Ming, K.; Kim, J.; Biondi, M. J.; Syed, A.; Chen, K.; Lam, A.; Ostrowski, M.; Rebbapragada, A.; Feld, J. J.; Chan, W. C. W. Integrated Quantum Dot Barcode Smartphone Optical Device for Wireless Multiplexed Diagnosis of Infected Patients. *ACS Nano* **2015**, *9*, 3060−3074.

(13) Klostranec, J. M.; Xiang, Q.; Farcas, G. A.; Lee, J. A.; Rhee, A.; Lafferty, E. I.; Perrault, S. D.; Kain, K. C.; Chan, W. C. W. Convergence of Quantum Dot Barcodes with Microfluidics and Signal Processing for Multiplexed High-Throughput Infectious Disease Diagnostics. *Nano Lett.* **2007**, *7*, 2812−2818.

(14) Zhang, Z.; Wang, Y.; Fan, C. H.; Li, C.; Li, Y.; Qian, L.; Fu, Y. M.; Shi, Y. Y.; Hu, J.; He, L. Asymmetric DNA Origami for Spatially Addressable and Index-Free Solution-Phase DNA Chips. *Adv. Mater.* **2010**, *22*, 2672−2676.

(15) Wang, G.; Leng, Y. K.; Dou, H. J.; Wang, L.; Li, W. W.; Wang, X. B.; Sun, K.; Shen, L. S.; Yuan, X. L.; Li, J. Y.; Sun, K.; Han, J. S.; Xiao, H. S.; Li, Y. Efficient Incorporation of Quantum Dots into Porous Microspheres Through A Solvent-Evaporation Approach. *ACS Nano* **2013**, *7*, 471−481.

(16) Sinkala, E.; Sollier-Christen, E.; Renier, C.; Rosàs-Canyelles, E.; Che, J.; Heirich, K.; Duncombe, T. A.; Vlassakis, J.; Yamauchi, K. A.; Huang, H. Y.; Jeffrey, S. S.; Herr, A. E. Profiling Protein Expression in Circulating Tumour Cells Using Microfluidic Western Blotting. *Nat. Commun.* **2017**, *8*, No. 14622.

(17) Wu, L. L.; Zhang, Z. L.; Tang, M.; Zhu, D. L.; Dong, X. J.; Hu, J.; Qi, C. B.; Tang, H. W.; Pang, D. W. Spectrally Combined Encoding for Profiling Heterogeneous Circulating Tumor Cells Using A Multifunctional Nanosphere-Mediated Microfluidic Platform. *Angew. Chem., Int. Ed.* **2020**, *59*, 11240−11244.

(18) Nong, R. Y.; Gu, J. J.; Darmanis, S.; Kamali-Moghaddam, M.; Landegren, U. DNA-Assisted Protein Detection Technologies. *Expert Rev. Proteomics* **2012**, *9*, 21−32.

(19) Fredriksson, S.; Dixon, W.; Ji, H.; Koong, A. C.; Mindrinos, M.; Davis, R. W. Multiplexed Protein Detection by Proximity Ligation for Cancer Biomarker Validation. *Nat. Methods* **2007**, *4*, 327−329.

(20) Burns, T. J.; Frei, A. P.; Gherardini, P. F.; Bava, F. A.; Batchelder, J. E.; Yoshiyasu, Y.; Yu, J. M.; Groziak, A. R.; Kimmey, S. C.; Gonzalez, V. D.; Fantl, W. J.; Nolan, G. P. High-Throughput Precision Measurement of Subcellular Localization in Single Cells. *Cytometry, Part A* **2017**, *91*, 180−189.

(21) Goltsev, Y.; Samusik, N.; Kennedy-Darling, J.; Bhate, S.; Hale, M.; Vazquez, G.; Black, S.; Nolan, G. P. Deep Profiling of Mouse Splenic Architecture with CODEX Multiplexed Imaging. *Cell* **2018**, *174*, 968−981.

(22) Agasti, S. S.; Liong, M.; Peterson, V. M.; Lee, H.; Weissleder, R. Photocleavable DNA Barcode-Antibody Conjugates Allow Sensitive and Multiplexed Protein Analysis in Single Cells. *J. Am. Chem. Soc.* **2012**, *134*, 18499−18502.

(23) Niu, R. J.; Song, C. Y.; Gao, F.; Fang, W. N.; Jiang, X. Y.; Ren, S. K.; Zhu, D.; Su, S.; Chao, J.; Chen, S. F.; Fan, C. H.; Wang, L. H. DNA-Based Origami Nanoprinting for the Assembly of Plasmonic Nanostructures with Single-Molecule Surface-Enhanced Raman Scattering. *Angew. Chem., Int. Ed.* **2021**, *60*, 11695−11701.

(24) Sun, L. L.; Shen, F. Y.; Xu, J.; Han, X.; Fan, C. H.; Liu, Z. DNA-Edited Ligand Positioning on Red Blood Cells to Enable Optimized T Cell Activation for Adoptive Immunotherapy. *Angew. Chem., Int. Ed.* **2020**, *59*, 14842−14853.

(25) Cui, M.-R.; Li, X.; Chen, H.; Xu, J. Smart Engineering of a Self-Powered and Integrated Nanocomposite for Intracellular MicroRNA Imaging. *CCS Chemistry* **2021**, *3*, 2063−2073.

(26) Yin, C.; Li, X. Z.; Wang, Y.; Liang, Y. Y.; Zhou, S.; Zhao, P. C.; Lee, C. S.; Fan, Q. L.; Huang, W. Organic Semiconducting Macromolecular Dyes for NIR-II Photoacoustic Imaging and Photothermal Therapy. *Adv. Funct. Mater.* **2021**, *31*, No. 2001453.

(27) Zhai, T. T.; Zheng, H. R.; Fang, W. N.; Gao, Z. S.; Song, S. P.; Zuo, X. L.; Li, Q.; Wang, L. H.; Li, J.; Shi, J. Y.; Liu, X. G.; Tian, Y.; Shen,

J. L.; Fan, C. H. DNA-Encoded Gold-Gold Wettability for Programmable Plasmonic Engineering. *Angew. Chem., Int. Ed.* **2022**, *61*, No. e202210377.
(28) Fournier-Bidoz, S.; Jennings, T. L.; Klostranec, J. M.; Fung, W.; Rhee, A.; Li, D.; Chan, W. C. W. Facile and Rapid One-Step Mass Preparation of Quantum-Dot Barcodes. *Angew. Chem., Int. Ed.* **2008**, *47*, 5577−5581.
(29) Xu, H. X.; Sha, M. Y.; Wong, E. Y.; Uphoff, J.; Xu, Y. H.; Treadway, J. A.; Truong, A.; O'Brie, E.; Asquith, S.; Stubbins, M.; Spurr, N. K.; Lai, E. H.; Mahoney, W. Multiplexed Snp Genotyping Using the Qbead System: A Quantum Dot-Encoded Microsphere-Based Assay. *Nucleic Acids Res.* **2003**, *31*, No. e43.
(30) Zhou, X.; Satyabola, D.; Liu, H.; Jiang, S.; Qi, X.; Yu, L.; Lin, S.; Liu, Y.; Woodbury, N. W.; Yan, H. Two-Dimensional Excitonic Networks Directed by DNA Templates as An Efficient Model Light-Harvesting and Energy Transfer System. *Angew. Chem. Int. Ed* **2022**, *61*, No. e202211200.
(31) Schweller, R. M.; Zimak, J.; Duose, D. Y.; Qutub, A. A.; Hittelman, W. N.; Diehl, M. R. Multiplexed in Situ Immunofluorescence Using Dynamic DNA Complexes. *Angew. Chem., Int. Ed.* **2012**, *51*, 9292−9296.
(32) Duose, D. Y.; Schweller, R. M.; Zimak, J.; Rogers, A. R.; Hittelman, W. N.; Diehl, M. R. Configuring Robust DNA Strand Displacement Reactions for in Situ Molecular Analyses. *Nucleic Acids Res.* **2012**, *40*, 3289−3298.
(33) Giedt, R. J.; Pathania, D.; Carlson, J. C. T.; McFarland, P. J.; del Castillo, A. F.; Juric, D.; Weissleder, R. Single-Cell Barcode Analysis Provides a Rapid Readout of Cellular Signaling Pathways in Clinical Specimens. *Nat. Commun.* **2018**, *9*, No. 4550.
(34) Agasti, S. S.; Wang, Y.; Schueder, F.; Sukumar, A.; Jungmann, R.; Yin, P. DNA-Barcoded Labeling Probes for Highly Multiplexed Exchange-PAINT Imaging. *Chem. Sci.* **2017**, *8*, 3080−3091.
(35) Kwak, M.; Herrmann, A. Nucleic Acid/Organic Polymer Hybrid Materials: Synthesis, Superstructures, and Applications. *Angew. Chem., Int. Ed.* **2010**, *49*, 8574−8587.
(36) Sundah, N. R.; Ho, N. R. Y.; Lim, G. S.; Natalia, A.; Ding, X. G.; Liu, Y.; Seet, J. E.; Chan, C. W.; Loh, T. P.; Shao, H. L. Barcoded DNA Nanostructures for the Multiplexed Profiling of Subcellular Protein Distribution. *Nat. Biomed. Eng.* **2019**, *3*, 684−694.
(37) Gires, O.; Pan, M.; Schinke, H.; Canis, M.; Baeuerle, P. A. Expression and Function of Epithelial Cell Adhesion Molecule EpCAM: Where Are We After 40 Years? *Cancer Metastasis Rev.* **2020**, *39*, 969−987.
(38) Iqbal, N.; Iqbal, N. Human Epidermal Growth Factor Receptor 2 (HER2) in Cancers: Overexpression and Therapeutic Implications. *Mol. Biol. Int.* **2014**, *2014*, No. 852748.
(39) Nakai, K.; Hung, M. C.; Yamaguchi, H. A Perspective on Anti-EGFR Therapies for Triple-Negative Breast Cancer. *Breast Cancer Res.* **2016**, *18*, 1609−1623.
(40) Mao, M.; Lin, Z.; Chen, L.; Zou, Z. Y.; Zhang, J.; Dou, Q. H.; Wu, J. C.; Chen, J. L.; Wu, M. H.; Niu, L.; Fan, C. H.; Zhang, Y. Q. Modular DNA-Origami-Based Nanoarrays Enhance Cell Binding Affinity Through the "Lock-and-Key" Interaction. *J. Am. Chem. Soc.* **2023**, *145*, 5447−5455.
(41) Wang, Y.; Gao, J.; Guo, X. D.; Tong, T.; Shi, X. S.; Li, L. Y.; Qi, M.; Wang, Y. J.; Cai, M. J.; Jiang, J. G.; Xu, C. Q.; Ji, H. B.; Wang, H. D. Regulation of EGFR Nanocluster Formation by Ionic Protein-Lipid Interaction. *Cell Res.* **2014**, *24*, 959−976.
(42) Fu, Y. M.; Zeng, D. D.; Chao, J.; Jin, Y. Q.; Zhang, Z.; Liu, H. J.; Li, D.; Ma, H. W.; Huang, Q.; Gothelf, K. V.; Fan, C. H. Single-Step Rapid Assembly of DNA Origami Nanostructures for Addressable Nanoscale Bioreactors. *J. Am. Chem. Soc.* **2013**, *135*, 696−702.
(43) Liu, X. G.; Zhao, Y.; Liu, P.; Wang, L. H.; Lin, J. P.; Fan, C. H. Biomimetic DNA Nanotubes: Nanoscale Channel Design and Applications. *Angew. Chem., Int. Ed.* **2019**, *58*, 8996−9011.
(44) Liu, S. L.; Jiang, Q.; Zhao, X.; Zhao, R. F.; Wang, Y. N.; Wang, Y. M.; Liu, J. B.; Shang, Y. X.; Zhao, S.; Wu, T. T.; Zhang, Y. L.; Nie, G. J.; Ding, B. Q. A DNA Nanodevice-Based Vaccine for Cancer Immunotherapy. *Nat. Mater.* **2021**, *20*, 421−430.
(45) Kuo, H. P.; Chuang, T. C.; Yeh, M. H.; Hsu, S. C.; Way, T. D.; Chen, P. Y.; Wang, S. S.; Chang, Y. H.; Kao, M. C.; Liu, J. Y. Growth Suppression of HER2-Overexpressing Breast Cancer Cells by Berberine Via Modulation of the HER2/PI3K/Akt Signaling Pathway. *J. Agric. Food Chem.* **2011**, *59*, 8216−8224.
(46) Tang, R.; Fu, Y. H.; Gong, B.; Fan, Y. Y.; Wang, H. H.; Huang, Y.; Nie, Z.; Wei, P. A Chimeric Conjugate of Antibody and Programmable DNA Nanoassembly Smartly Activates T Cells for Precise Cancer Cell Targeting. *Angew. Chem., Int. Ed.* **2022**, *61*, No. e202206529.
(47) Xu, F.; Xia, Q.; Ye, J.; Dong, L.; Yang, D. L.; Xue, W.; Wang, P. F. Programming DNA Aptamer Arrays of Prescribed Spatial Features with Enhanced Bioavailability and Cell Growth Modulation. *Nano Lett.* **2022**, *22*, 9935−9942.
(48) Qin, W. W.; Chen, L.; Wang, Z. R.; Li, Q.; Fan, C. H.; Wu, M. H.; Zhang, Y. Q. Bioinspired DNA Nanointerface with Anisotropic Aptamers for Accurate Capture of Circulating Tumor Cells. *Adv. Sci.* **2020**, *7*, No. 2000647.
(49) Yu, M.; Bardia, A.; Wittner, B.; Stott, S. L.; Smas, M. E.; Ting, D. T.; Isakoff, S. J.; Ciciliano, J. C.; Wells, M. N.; Shah, A. M.; Concannon, K. F.; Donaldson, M. C.; Sequist, L. V.; Brachtel, E.; Sgroi, D.; Baselga, J.; Ramaswamy, S.; Toner, M.; Haber, D. A.; Maheswaran, S. Circulating Breast Tumor Cells Exhibit Dynamic Changes in Epithelial and Mesenchymal Composition. *Science* **2013**, *339*, 580−584.
(50) Wade, O. K.; Woehrstein, J. B.; Nickels, P. C.; Strauss, S.; Stehr, F.; Stein, J.; Schueder, F.; Strauss, M. T.; Ganji, M.; Schnitzbauer, J.; Grabmayr, H.; Yin, P.; Schwille, P.; Jungmann, R. 124-Color Super-Resolution Imaging by Engineering DNA-PAINT Blinking Kinetics. *Nano Lett.* **2019**, *19*, 2641−2646.
(51) Zhai, T. T.; Li, Q.; Shen, J. L.; Li, J.; Fan, C. H. DNA Nanostructure-Encoded Fluorescent Barcodes. *Aggregate* **2020**, *1*, 107−116.

https://doi.org/10.1021/acsnano.5c18968
ACS Nano 2026, 20, 5904−5917